Updated modelling and refined absolute parameters of the oscillating eclipsing binary AS Eri⋆

P. Lampens[1]†,D. Mkrtichian[2], H. Lehmann[3], K. Gunsriwiwat[2], and L. Vermeylen[1]
[1]Royal Observatory of Belgium, Ringlaan 3, Brussel 1180, Belgium
[2]National Astronomical Research Institute of Thailand, 260 Moo 4, T. Donkaew, A. Maerim, Chiangmai, 50180, Thailand
[3]Thüringer Landessternwarte, Tautenburg, Germany

Accepted XXX. Received YYY; in original form ZZZ

ABSTRACT

We present a new study of the Algol-type eclipsing binary system AS Eri based on the combination of the MOST and TESS light curves and a collection of very precise radial velocities (RVs) obtained with the spectrograph HERMES operating at the *Mercator* telescope, Observatorio Roque de los Muchachos, La Palma, and the TCES instrument operating at the *Alfred Jensch* telescope of the Thüringer Landessternwarte, Tautenburg. The primary component is an A3 V-type pulsating, mass-accreting star (or oEA star). We fitted the light and RV data with the modelling tool PHOEBE, and determined the best-fitting model for this binary adopting the configuration of a semi-detached system. The orbital period has been revised and refined using a recent (O-C) analysis and the phase shift detected between both light curves to the value of 2.6641496 ± 0.0000001 days. The absence of any cyclic variation in the (O-C) residuals confirms the long-term stability of the orbital period. Furthermore, we show that the models derived for each light curve separately entail small differences, e.g. in the temperature parameter $T_{eff,2}$. The high quality of the proposed solutions is illustrated by the residuals after subtraction of the best model. We obtained the following absolute parameters for the components based on all data sets: L_1 = 14.125 ± 0.008 $L_\odot$, M_1 = 2.014 ± 0.004 $M_\odot$, R_1 = 1.733 ± 0.006 $R_\odot$, log g_1 = 4.264 ± 0.005 and L_2 = 4.345 ± 0.003 $L_\odot$, M_2 = 0.211 ± 0.001 $M_\odot$, $R_\odot$, R_2 = 2.19 ± 0.01 $R_\odot$, log g_2 = 3.078 ± 0.003 together with $T_{eff,2}/T_{eff,1}$ = 0.662 ± 0.002. Although the orbital period appears to be stable on the long term, we show that the light curve shape is affected by a years-long modulation which is most probably due to the magnetic activity of the cool companion.

Key words: Stars: binaries: eclipsing – Stars: binaries: spectroscopic – technique: photometry – technique: spectroscopy – Stars: fundamental parameters – Stars: mass loss – Stars: oscillations

1 INTRODUCTION

Eclipsing systems are essential objects for our understanding of the properties of stars as well as stellar systems. Well detached, double-lined, eclipsing systems offer the advantage of model-independent fundamental parameters of their components which can be used as direct constraints in the search for relevant models of stellar structure and evolution across the HR-diagram (Torres et al. 2010). An additional constraint may come from the equal age, equal composition requirement. Their modelling furthermore allows to derive stellar surface properties such as reflection, gravity brightening and limb darkening coefficients, tidal flattening (ellipsoidality), surface inclinations (spin-orbit alignment) and even mode identifications obtained from a dynamical screening of the pulsating surfaces during eclipses (using the spatial filtering or dynamical eclipse mapping methods, e.g. hereunder) (Prša et al. 2016; Horvat et al. 2018).

Eclipsing systems with pulsating components are most interesting study targets: not only do they provide the fundamental component properties needed in the search for a precise asteroseismic model, but they also undergo a series of phenomena that are intrinsically linked to the gravitational forces acting on the components, for example tidal effects and mass transfer stages. These phenomena can and will influence the stellar interiors and surfaces, including the pulsations (Lampens 2021). The orbital configuration plays a role too since different kinds of tidal interactions are observed in short-period, circular versus eccentric systems. Tides can generate stellar pulsations, e. g. by a resonance mechanism such as in the eccentric 'heartbeat' systems (Fuller & Lai 2012; Cheng et al. 2020). In turn, tidally excited non-radial oscillations can also affect the evolution of close binaries (Aerts 2021, Sect.IV.F and references therein).

The first pulsating mass-accreting components of semi-detached Algol-type systems, AB Cas (Tempesti 1971) and Y Cam (Broglia 1973), were discovered in the 1970's. However, understanding that they belong to a new class of pulsating stars was delayed until the early 2000's, when Mkrtichian et al. (2002, 2004) classified them under the name 'oEA stars' as a special class of short-period main-sequence mass-accreting pulsators that are evolutionary different from the classical δ Scuti stars found in detached eclipsing systems.

⋆ Based on observations made with the *Mercator* telescope, operated by the Flemish Community at the Observatorio del Roque de los Muchachos of the Instituto de Astrofísica de Canarias, La Palma, Spain, and the *Alfred Jensch* telescope at the Thüringer Landessternwarte, Tautenburg, Germany.

† E-mail: patricia.lampens@oma.be

Since this recognition, the number of mass-accreting components discovered from the ground gradually increased, reaching almost 80 members in 2018 (Mkrtichian et al. 2018). Recently, this number increased by a factor of about two thanks to the results of the TESS mission (Mkrtichian et al., in prep.)

These close binary systems experience (still) on-going non-stationary mass transfer via the inner Lagrange L1 point into the atmosphere of the pulsating component. Mass accretion results in changes of the radius, mass, density as well as of the short-scale response of the pulsating star which depend on the mass-accretion rate. It is still a matter of debate whether or not the mass transfer stage in Algol-type systems is fully conservative or not (Budding & Butland 2011; Lehmann et al. 2018). So far, RZ Cas is the best investigated oEA system which makes it suitable for exploring the interaction between mass exchange and pulsations. Lehmann et al. (2020) detected two opposite, cool and dark spots on the surface of the secondary component facing the Lagrangian points L1 and L2 from their long-term spectroscopic study of RZ Cas lasting from 2001 to 2017. They showed that the spot sizes varied in an opposite way with a characteristic time scale of 9 years (already reported from the (O-C) variations by Mkrtichian et al. (2018)), while the time scale of the L2 spot migration was found to be close to 18 years. They interpreted the 9-yr time scale as half of an 18-yr magnetic dynamo cycle of the cool companion. They also concluded that the mass-transfer rate is controlled by the variable depth of the Wilson depression in the magnetic spot around L1. These results illustrate the importance of an accurate determination of the fundamental parameters of components of eclipsing binary systems and their surface structures via precise photometric and spectroscopic analyses.

AS Eri (HD 57167, HIP 35487, HR 2788, TYC 5965-2336-1) is an 8th-magnitude, semi-detached eclipsing and double-lined spectroscopic binary (Popper 1973) of spectral type A3 V + K0 III with the light ephemeris given by Kreiner (2004, 2005) :

$$\text{Min. (HJD)} = 2452502.108 + E \times 2^{\text{d}}.664145.$$

Koch (1960) and Lindsay & Cillié (1960) obtained the first photoelectric light curves of AS Eri in the filters blue and yellow. Based on their data and Koch (1960)'s photometric solution, Hutchings & Hill (1971) derived two possible models with the secondary component distorted close to its Roche limit. Popper (1973) and Van Hamme & Wilson (1984) were the first ones to derive a full set of orbital parameters for the system. Alicavus (2020) derived the absolute parameters by analysing the light curve from the Transiting Exoplanet Survey Satellite (TESS). According to Eggleton & Kiseleva-Eggleton (2002), this system evolved to its present configuration after a substantial loss of angular momentum.

Rapid pulsations with a period of 24.4 min (f = 59.0312 d^{-1}), attributed to its primary component, were discovered by Gamarova et al. (2000). Later, Mkrtichian et al. (2004) confirmed the 24.4 min period and reported multiperiodic oscillations with additional frequencies of 62.5631 and 61.6743 d^{-1}. AS Eri is one of the first five semi-detached eclipsing binary systems with δ Scuti-type pulsations assigned to the class of oEA stars. Mkrtichian et al. (2004) proposed that, given their high inclination, the oEA systems are prime candidates for the detection and analysis of non-radial high-degree sectoral pulsations as well as for applying the method of 'spatial filtering' for mode identification during the eclipses (Gamarova et al. 2003; Rodríguez et al. 2004). In particular, the orbital-to-pulsation period ratio, $P_{\rm orb}/P_{\rm puls}$, of ~157 indicates that AS Eri A is particularly interesting for an in-depth analysis of its pulsational behaviour.

Glazunova et al. (2008) measured the rotational velocities of 23 eclipsing and spectroscopic binary systems using the techniques of Least-Squares Deconvolution (LSD) and Fourier analysis of the line profiles. They obtained $v \sin i$'s of 36 ± 3 and 40 ± 3 km s^{-1}, respectively for the primary and the secondary component of AS Eri.

Narusawa (2013) carried out an abundance analysis of the primary component of AS Eri based on spectral data obtained with the High Dispersion Spectrograph (R ~ 72 000) at the Subaru telescope. He reported underabundances of -0.66, -0.60, -0.57, -0.48, and -0.31 dex in respectively Fe, Ca, Mg, Ti, and Cr.

In this work, we will determine the best-fitting model for the system based on two sets of space-based light curves supplemented by a well-distributed series of recently acquired, high-resolution spectroscopic data. A detailed pulsational analysis of AS Eri based on the space-based data (MOST and TESS), multi-site ground-based photometry as well as complementary high-resolution spectroscopy will be presented in a follow-up paper.

2 OBSERVATIONS AND DATA REDUCTION

2.1 The radial velocity data

High-resolution spectra of AS Eri were collected in the years 2011, 2014 and 2015 for phase-resolved radial velocity monitoring. The observations were performed with the high-resolution fibre-fed échelle spectrograph HERMES (High Efficiency and Resolution Mercator Echelle Spectrograph, Raskin et al. (2011)) mounted at the focus of the 1.2-m *Mercator* telescope located at the international observatory Roque de los Muchachos (La Palma (LP), Spain). The instrument is operated by the University of Leuven under the supervision of the HERMES Consortium. It records the optical spectrum in the range λ = 377 - 900 nm across 55 spectral orders in a single exposure. The resolving power in the high-resolution mode is R = 85 000. Technical details and the performance of the instrument are described in (Raskin et al. 2011). We also used the TCES spectrograph[1] mounted at the Coudé focus of the 2-m *Alfred Jensch* telescope at the Thüringer Landessternwarte (TLS), Tautenburg. The instrument is a high-resolution échelle spectrograph and covers the wavelength range 445 - 755 nm with a resolving power R = 58 000 in combination with the NBI camera.

In total, we acquired 164 HERMES spectra in the years 2011, 2014 and 2015 whereas 166 TLS spectra were collected in 2015. The radial velocities (RVs) were determined twice making use of 163 normalized HERMES spectra and 160 normalized TCES spectra (7 spectra were omitted because of low S/N or artefacts), by one of us (HL) using his implementation of TODCOR which computes a two-dimensional (2D) cross-correlation (Mazeh & Zucker 1994), as well as by using another implementation of TODCOR first applied in the study of AU Mon (Desmet et al. 2010). We also derived uncertainties on the component RVs of all the HERMES spectra using the latter implementation of TODCOR. A composite (A2+G2)-model spectrum with a (fixed) $v \sin i$ pair of (35, 40) km s^{-1} was used for reference. We next computed the standard deviations obtained from the RVs derived from 14 different spectral regions of width approx. 100 Å chosen within the interval 4150-5700 Å of the normalized HERMES spectra. We stress the

[1] https://www.tls-tautenburg.de/TLS/index.php?id=31&L=1

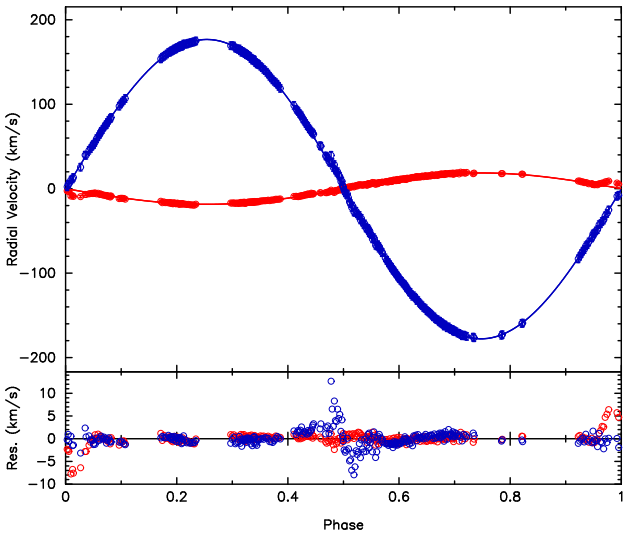

Figure 1. Component radial velocities and pure RV-based orbital solution. The Rossiter-McLaughlin effect is clearly present in the residual data.

fact that the individual RVs derived in both cases are fully consistent with each other. Hereafter, we will use the RVs determined by HL. Table A1 lists the Julian dates of the available spectroscopic observations and the corresponding RVs for each component. A preliminary orbital solution based on all RVs collected with both spectrographs was computed (see col. 2 of Table 1 and Fig. 1). Note that the Rossiter-McLaughlin (RML) effect was not modelled at this stage.

The component RVs were used as input for a simultaneous modelling study together with the MOST light curve (see Sect. 2.2). We used the eclipsing binary modelling software PHOEBE (Prša et al. 2011), initially without the estimated uncertainties, later with the standard deviations derived for the HERMES spectra complemented by estimated mean uncertainties for the TCES spectra (respectively 1.25 and 2.5 km s^{-1} for components A and B). For the MOST light curve, a mean standard error of 0.004 (~ 4 mmag) was derived from the scatter for flat portions of the light curve during the phases of light maximum and applied (see also later when the residuals are displayed). During the first modelling experiments, the light ephemeris from Kreiner (2005) was adopted to compute the phases:

$$\text{Min.(HJD)} = 2452502.108 + E \times 2^{\text{d}}.664145. \quad (2.1)$$

We remark that there is no reason to suspect a change of the orbital period from the (O-C) diagram published in the on-line Atlas of (O-C) Diagrams of Eclipsing Binaries (*http://www.as.up.krakow.pl/ephem*).

2.2 The space-based data sets

We used two sets of light curves that were obtained respectively by the satellite missions MOST (Ricker et al. 2016) and TESS (Walker et al. 2003). The MOST data set consists of 3875 relative magnitudes obtained in the MOST bandpass acquired between 2013, Oct. 10 and 2013, Nov. 20 ((BJD - 2 400 000) 56575.512841250 – 56616.517707390). We converted the original data set expressed in relative mag to normalised flux (with respect to maximum light) and removed one outlier.

The TESS data comprise 15936 data points in TESS light obtained in a single run from 2018, Oct. 19 to 2018, Nov. 14 (Sector 4, (BJD - 2 400 000) 58410.90617810 – 58436.83853767). We used the SAP (Simple Aperture Photometry) flux and its error, normalised and detrended the data, and removed three outlying data points. The light curves were phased against the published orbital period of 2.664145 d for a first check, confirming that both phase-folded plots looked good.

An additional and more recent light curve was acquired by TESS during the run from 2020, Oct. 22 to 2020, Nov. 16 (Sector 31, (BJD - 2 400 000) 59144.51980161 – 59169.94926016). We did not use this light curve comprising 16156 SAP fluxes for the determination of the binary model. Instead, we will use it to verify the final solution obtained from the former data sets to conclude on the long-term stability of the light curve in Sect. 6.

3 LIGHT AND RADIAL VELOCITY MODELLING

We used the eclipsing binary modelling software PHOEBE-1.0 (legacy, dd. 08/07/2012, *http://www.phoebe-project.org*). PHOEBE-1.0 is based on the widely known Wilson-Devinney method (Wilson & Devinney 1971). The code allows to simultaneously model the light and radial velocity curves of eclipsing binary systems using the full astrophysical information contained in the atmospheric models assuming a given configuration for the binary (Prša & Zwitter 2005). Here, we chose the semi-detached configuration with the secondary star filling its Roche lobe (MODE=5) and the preliminary orbital solution based on two sets of component RVs (Table 1, col. 2) in search of a first best-fitting model. The adopted orbital period was initially 2.664145 days (see Sect. 4). For the relative (passband-related) errors, we adopted 0.01 for the MOST light curve and 1.0 for the TODCOR RVs. The colours of the primary component have been evaluated by Popper (1973): he found (B - V) = +0.08. The primary is of spectral type A1 V or A3 V. We fixed the effective temperature of the primary component accordingly to the value of 8500 K. The surface albedo's, the gravity brightening of the primary component and the limb darkening coefficients (log law) were fixed to the standard values. The code provides the physical parameters of the components together with the orbital solution and formal errors from a combined, weighted least-squares analysis. Table 1 (col. 4) shows the revised orbital elements adopting the best-fitting solution considering the uncertainties and including two reflection effects. Fig. 2 (left and right) illustrates the light curve solution including the MOST model as well as the quality of the fit (illustrated by a plot of the residuals) using the MOST light curve.

Table 2 presents the orbital elements derived from the two best-fitting solutions considering the uncertainties and obtained from a modelling with PHOEBE-1.0 (including two reflection effects): the solutions a) without (left col.) and b) with the TESS light curve (right col.). Fig. 3 (left and right) illustrates the light curve solution including the TESS model as well as the quality of the fit (illustrated by a plot of the residuals) using both light curves. We used the same relative error of 0.01 for the TESS light curve. Since the TESS data (SAP flux) are very numerous (N = 15542), they outnumber the MOST data. The best-fitting solution which fits well all the data sets is thus heavily weighted toward the TESS light curve. In order to verify the stability of the orbital elements, a comparison with and without it was needed. We see that the final solution using the TESS light curve is somewhat different from the solution which was based on the MOST light curve. This concerns, for example, the epoch (T) and the inclination (i) implying a small though significant

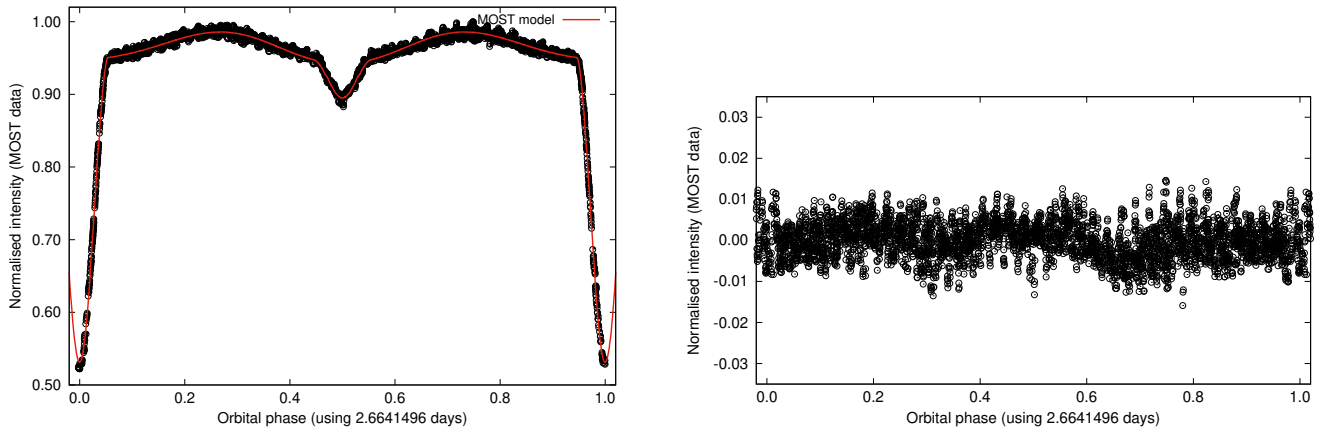

Figure 2. Left: The MOST light curve and the corresponding model (solid red line) plotted against the orbital phase. Right: The residuals after model subtraction plotted against the orbital phase.

Table 1. Orbital elements with formal errors and physical parameters of AS Eri, Col. 2) based on 323 newly acquired spectra (see Fig. 1). Col. 3) According to Van Hamme & Wilson (1984).

Orbital element	This work	VH&W
P (days)	2.6641534 ± 0.0000038	2.664152
T	55831.078 ± 0.079	28538.066
e	0.0107 ± 0.0021	null (fixed)
i (°)	undef.	80.451
ω (rad)	4.99 ± 0.19	undef.
$V_{01=02}$ (km s^{-1})	11.622 ± 0.069	11.70 ± 0.17
q	0.10470 ± 0.00067	0.1069 ± 0.0014
K_1 (km s^{-1})	18.55 ± 0.11	—
K_2 (km s^{-1})	177.21 ± 0.42	—
a_A.sin i (A.U.)	0.00454 ± 0.00003	—
a_B.sin i (A.U.)	0.0434 ± 0.0001	—
mass$_A$.sin i^3 ($M_\odot$)	1.874 ± 0.013	—
mass$_B$.sin i^3 ($M_\odot$)	0.196 ± 0.002	—
rms (comp A & B) (km s^{-1})	1.27 & 1.80 resp.	—

change of some orbital parameters. Such a change might be caused by the presence of a third component (see Van Hamme & Wilson 1984, hereafter VH&W) who concluded from their modelling on the possible existence of third light) or by apsidal motion (less probable in the case of a circular orbit). With respect to the phase shift (see the discrepancy in T), this may be easily explained by the need for an increase of order 4.5e-06 d in the orbital period. Such a correction is of the same order as the uncertainty on the period from each space light curve. A more accurate orbital period is difficult to assess from a multi-dimensional least-squares fitting because of the correlations between the free parameters. The result of further analysis (based on letting only one parameter free) is described in Sect. 4.

4 THE REVISED ORBITAL PERIOD

Before the final modelling work, we computed a revised light ephemeris based on all the times of minima collected with the photoelectric technique (E) and the CCD (C) from the Lichtenknecker Database of the *Bundesdeutsche Arbeitsgemeinschaft für Veränderliche Sterne e.V. (BAV)*, together with new times of minima determined by us from the MOST and TESS light curves. We furthermore included four unpublished times of minima obtained with the robotic telescopes PROMPT-8 at Cerro Tololo Observatory, Chile, the SSO-2 and SSO-3 at Siding Springs Observatory, Australia, and the R-COP at Perth Observatory, New-Zealand. In this way, we gathered 104 times of primary and 30 times of secondary minima. Table B1 lists all acquired times of minima. From a linear fit to these higher quality timings, we obtained the updated light ephemeris:

$$\text{Min.(HJD)} = 2456575.58990\ (\pm\ 3) + \text{E} \times 2\overset{\text{d}}{.}66415018\ (\pm\ 3) \quad (4.1)$$

and adopted this new period to (re)compute the phases. The corresponding diagram of (O-C) residuals (Table B1, col.4), including all the data points, is presented in Fig. 4.

Next, by fitting only the initial epoch T of each light curve, we derived an accurate epoch of phase 0 for each data set. Since the difference between both initial epochs equals 1835.599061 d, the total phase shift of -0.00041 d and a refined period of 2.6641496 ± 0.0000001 d is obtained adopting the closest integer number of cycles (E = 689). This revised orbital period removes the previously reported phase discrepancy between both space light curves and was subsequently adopted during the final minimization run.

5 LIGHT AND VELOCITY MODELLING: THE FINAL RUN

For the final modelling experiment, we adopted the orbital period of 2.6641496 d (enabling to bridge the gap between both light curves without phase shift) and we fixed the longitude of periastron to 4.70 rad (a value taken from the previous solutions, considering that it has little effect since the eccentricity is very small) and the filling factor f_1 to 1.1 - 1.2 (this provides an excellent match between the RV data and the model for the amplitude of the RML effect of

Table 2. Orbital and physical parameters with formal errors, resp. based on the MOST light curve and the component RVs, and based on the same with the TESS light curve added.

Orbital element	*Phoebe-1.0* (w/o TESS)	*Phoebe-1.0* (with TESS)
P (days)	2.664145 (fixed)	2.664145 (fixed)
T	52502.11297 ± 0.00007	52502.11613 ± 0.00002
e	0.00125 (free > fixed)	0.00125 (fixed)
i (°)	80.3250 ± 0.0056	80.4261 ± 0.0008
ω (°)	4.696 ± 0.56 (free > fixed)	4.696 (fixed)
$V_{01=02}$ (km s^{-1})	11.899 ± 0.028	11.899 (fixed)
q	0.10486 ± 0.00013	0.10486 (fixed)
$T_{eff,B}$ (K)	5609 ± 8	5609 (fixed)
f_1	1.20 (fixed)	1.20 (fixed)
grb_2	0.077 ± 0.002 (free > fixed)	0.077 (fixed)
Ω_1	6.1843 ± 0.0007	6.2251 ± 0.0003
HLA_1 (L_1 (MOST))	10.1988 ± 0.0010	10.2028 ± 1.48
HLA_2 (L_1 (TESS))	undef.	8.9955 ± 0.0003
A ($R_\odot$)	10.5647 ± 0.0060	10.5647 (fixed)
$mass_A$ ($M_\odot$)	2.0176	2.0176
$mass_B$ ($M_\odot$)	0.2116	0.2116
R_A ($R_\odot$)	1.742	1.732
R_B ($R_\odot$)	2.198	2.198
χ^2_{tot}	1117	10.4e+09

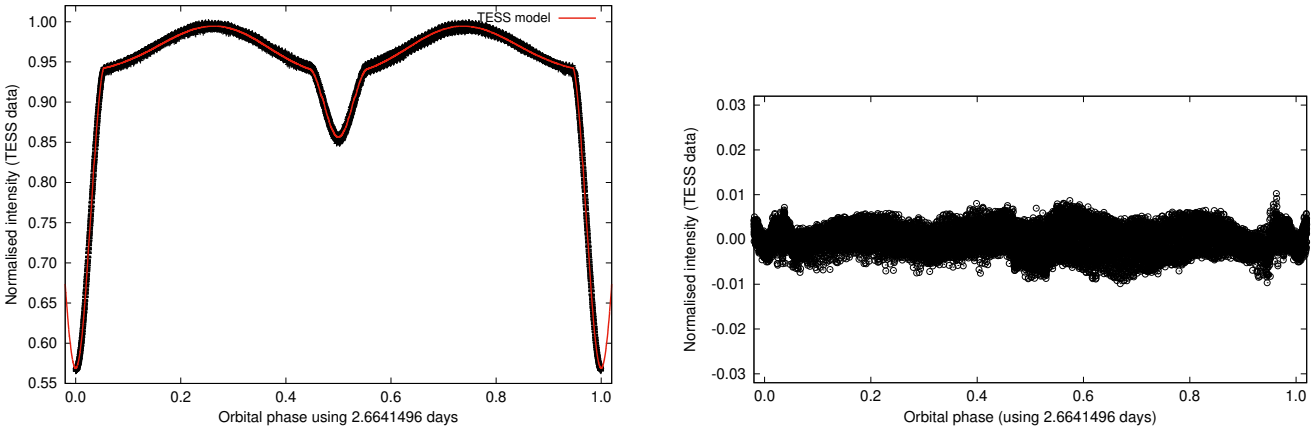

Figure 3. Left: The detrended TESS light curve and its corresponding model (solid red line) plotted against the orbital phase. Right: The residuals after model subtraction plotted against the orbital phase.

comp A, see Fig. 7). We performed a new search for the best-fitting model twice: first, with the MOST light curve and the component RVs and then, with both (MOST+TESS) light curves and the component RVs. Here, we adopted the relative errors of 0.1 and 1.0 for the light curves and the TODCOR RVs, respectively. The logarithmic limb darkening law and two reflection effects were included in all our computations. All remaining parameters (except for $T_{eff,1}$) were set free at one point, though we used a stepwise approach to avoid the presence of strong correlations during the minimization process.

Table 3 presents the orbital and physical parameters with their formal errors associated to the best-fitting solutions obtained from a modelling with PHOEBE-1.0. We list the final solution a) without (left col.) and b) with the TESS light curve (right col.). Figure 2 illustrates the best-fitting binary model and the quality of the fit (illustrated by a plot of the residuals) based on the MOST light curve. Figure 3 illustrates the best-fitting binary model and the quality of the fit (illustrated by a plot of the residuals) based on the TESS light curve. The residuals are in very good agreement with the estimated standard deviations of the respective data sets and the possible short-term drifts. The TESS light residuals are somewhat noisier than expected, because detrending of the data was performed linearly on the long-term time scale (and small short-term drifts may still occur) and also because of the existence of δ Scuti-type pulsations (see Sect. 1).

Table 3. Orbital and physical parameters with their formal errors from *Phoebe-1.0* based on the MOST light curve with the RVs (col. 2), and on the same but with the TESS light curve added (col. 3).

Orbital element	*Phoebe-1.0* (w/o TESS)	*Phoebe-1.0* (with TESS)
P (days)	2.6641496 (fixed)	2.6641496 (fixed)
T	56575.58972 ± 0.00007	58411.18970 ± 0.00002
e	0.00125 (free > fixed)	0.00063 ± 0.00008
i (°)	80.3246 ± 0.0063	80.4287 ± 0.0012
ω (rad)	4.70 ± 0.56 (free > fixed)	4.70 (fixed)
$V_{01=02}$ (km s^{-1})	11.921 ± 0.028	11.918 ± 0.034 (> fixed)
q	0.10468 ± 0.00032	0.10467 ± 0.00030 (> fixed)
$T_{eff,B}$ (K)	5482 ± 26	5646 ± 7
f_1	1.20 (fixed)	1.10 (fixed)
gb_2	0.077 ± 0.002 (free > fixed)	0.075 ± 0.001
Ω_1	6.2479 ± 0.0011	6.2131 ± 0.0003
HLA_1 ($L_{1,MOST}$)	10.1953 ± 0.0013	9.0024 ± 1.44
HLA_2 ($L_{1,TESS}$)	undef.	8.9937 ± 0.0004
A ($R_\odot$)	10.5535 ± 0.0059	10.5509 ± 0.0072 (> fixed)
$mass_A$ ($M_\odot$)	2.0115	2.0124
$mass_B$ ($M_\odot$)	0.2106	0.2106
R_A ($R_\odot$)	1.722	1.729
R_B ($R_\odot$)	2.195	2.195
χ^2_{tot}	1085	10.3e+07

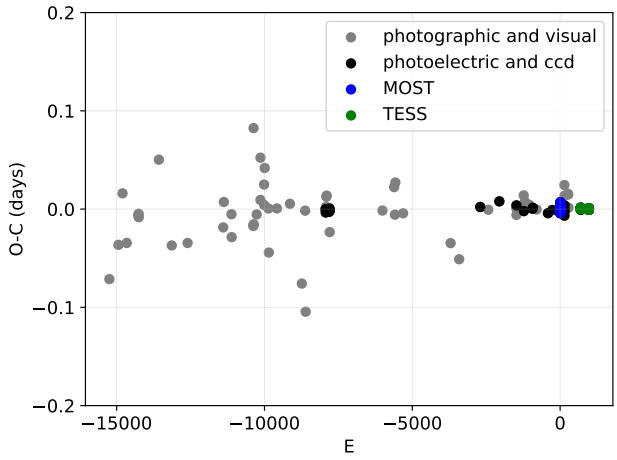

Figure 4. Updated O-C diagram of AS Eri. Different symbols illustrate the various types of times of minima. One obvious outlier (> +0.3 d) was removed.

6 THE MODELS

We present the solution associated to each light curve (LC), i.e. the models for the MOST and the TESS data sets together in Fig. 5. It can be seen from Fig. 5 that a different LC model from each minimization was obtained. The difference between the LC solutions is not only due to the choice of the passband. This is also evidenced by the small though significant changes in the values of the inclination (i), the gravitational potential (Ω_1), and the effective temperature of comp B ($T_{eff,2}$) in Table 3. The difference of 200 K in the temperature of comp B does not seem large in se, but the LC models are clearly distinct. However, in both solutions, the same RV model was used. The RV data and model are shown for both components in Fig. 6 (left panel), whereas Fig. 7 shows the same in a closer look for comp A only. The residual data for both components are also presented in Fig. 6 (right panel). In the latter, we can see that the RV residuals of comp B display small systematic shifts with respect to the final solution, e.g. at the orbital phases ~ 0.1, in the vicinity of 0.5 and ~ 0.9. In order to represent the component RVs with the latter solution in the finest possible details, we had to introduce a small change in eccentricity, i.e. increasing its value from near-zero to almost that of Table 1. We adopted an eccentricity of 0.01063. This small increase in eccentricity allowed us to significantly reduce the systematics in the residuals of the RVs of comp B (at the phases ~ 0.1 and 0.9), but the slightly larger eccentricity affects the LC model such that the quality of the fit to the TESS data is no longer as good as before (i.e. χ^2_{tot} = 12.5e+07). Thus the final solution defines an almost circular orbit, whereas the fit to the RV curve of comp B can be improved adopting a small eccentricity (e.g. the one derived from a pure RV-based orbit). We conclude that the near-zero eccentricity found during the final modelling experiment is caused by the dominance of the high-quality TESS LC over the RV data set.

We provide the fundamental component parameters and the relative shape (or radii) of each component from the final solution in Table 4. The physical properties of each component were determined using all the data sets, including the TESS light curve from Sector 4, fitted together with an orbital period of 2.6641496 d.

Finally, since the conclusion is that the LC model changed over the course of 5 years (i.e. the time span between the missions MOST and TESS), we decided to verify our solution based on the TESS light curve from Sector 4 against the more recent one from Sector 31. Figure 8 illustrates this comparison. We observe that primary minimum is deeper again and that the more recent light curve is no longer agreeing with the TESS model. Its shape follows more closely that of the MOST model. From this, we deduce that the

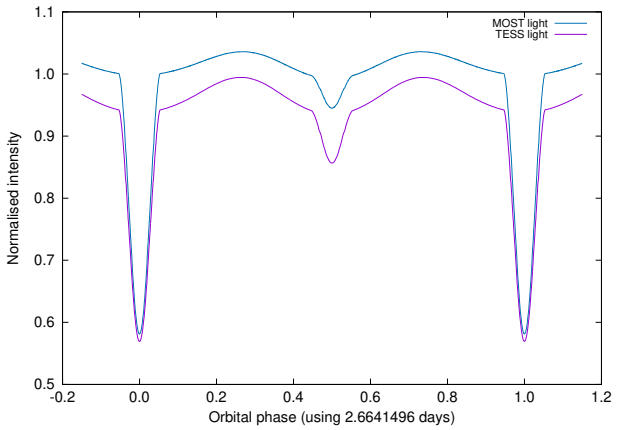

Figure 5. Light curve models for AS Eri.

Table 4. Stellar parameters based on the final binary model. The relative radii expressed in units of the semi-major axis A are listed as 'radius'.

Mass ($M_\odot$) ± error	Radius ($R_\odot$) ± error	M_{Bol} (mag) ± error	log g (cgs) ± error
M_1 = 2.014 ± 0.004	R_1 = 1.733 ± 0.006	$M_{Bol,1}$ = 1.865 ± 0.008	log g_1 = 4.264 ± 0.005
M_2 = 0.211 ± 0.001	R_2 = 2.19 ± 0.01	$M_{Bol,2}$ = 3.145 ± 0.008	log g_2 = 3.078 ± 0.003
radius (pole)	radius (point)	radius (side)	radius (back)
r_1 = 0.1634	r_1 = 0.1643	r_1 = 0.1641	r_1 = 0.1642
r_2 = 0.1924	r_2 = 0.2860	r_2 = 0.2000	r_2 = 0.2310

light curve shape varies intrinsically over a time span of a few years.

7 DISCUSSION AND CONCLUSIONS

We determined new system and stellar parameters for the oscillating Algol-type eclipsing binary AS Eri based on combined photometry and spectroscopy, namely, two photometric data sets from the MOST and TESS missions, as well as a large series of component radial velocities obtained from high-resolution spectroscopy. The final solution was obtained through a series of minimizations, where a comparison with previous studies was done when possible as an independent verification of our results. Here, we performed the final modelling using the refined orbital period of 2.6641496 d which was needed to remove the phase gap between the two light curves from space. The final model agrees very well with the high-quality data of the TESS light curve. We also showed that this solution does not entirely fit the MOST light curve as some of the parameters such as the effective temperature of comp B, the inclination (i) and the gravitational potential of comp A (Ω_1) needed a significant correction. Both LC models indicate an almost circular orbit. However, the RV data are better represented with a small non-zero eccentricity, which indicates that the space photometric and ground-based spectroscopic data do not fully agree with each other. Since the uncertainties of the RVs were cautiously estimated, this did not prevent us from finding an optimum solution with all three data sets combined into one minimization run. The residuals obtained after subtraction of the best model derived in this work will enable to study the pulsation properties of AS Eri with a higher accuracy and more details than hitherto possible.

We conclude with the following remarks:
- AS Eri is a system whose mass ratio (q) is very accurately known because both techniques contribute to its determination. Note that the new q is close to that derived by Van Hamme & Wilson (1984).
- The final solution agrees overall quite well with the first solution proposed by VH&W, except for $T_{eff,2}$ which is found to be hotter than previously thought, implying a temperature difference of 600 to 800 K between the components. This discrepancy is not due to the release of the gravity brightening parameter, gb_2, which has profoundly changed from the default value to a plausible 0.08 (VH&W derived a similar value, see also the case of KIC 9851944 by Guo et al. (2016)). The fact that they obtained a different $T_{eff,2}$ may look surprising, but could be possibly due to using an initial value based on older findings (Koch 1960; Hutchings & Hill 1971).
- The final solution corresponds to the semi-detached case where the secondary fills its Roche lobe. The primary component belongs to the main sequence whereas the secondary is an evolved giant star. The relative stellar radii are not compatible with those of VH&W either, as the mean radius of comp A is about 10% larger than theirs (we allowed for non-synchronous rotation, i.e. f_1 = 1.10-1.20, which enabled us to fit the observed RLM effect).
- The cyclic modulations of the orbital periods observed in a majority of Algol-type systems with late-type, Roche-lobe filling components can be explained by the magnetic activity of their cool companions (Applegate 1992). In the case of AS Eri, we report the high stability of its orbital period based on the absence of any short-term cyclic variation in its (O-C) diagram, which possibly indicates weak magnetic activity of the secondary component. On the other hand, we showed that the shape of the light curve significantly varies over a time scale of a few years (Fig. 8). Therefore, while the orbital period appears to be stable on the long term, we conclude that the light curve is affected by a years-long modulation which is most probably reflecting the magnetic activity cycle of the cool companion. The fact that the orbital period is stable does not contradict this result.
- Although the RML effect is well evidenced in the RV residuals of both components (see bottom panel in Fig 1 and also Fig. 7), we are currently unable to detect any asymmetry in the residuals of the primary component. Such asymmetry can be caused by an asymmetrical attenuation of the stellar disk by the gas stream and/or an inhomogeneous distribution of the accreted gas around the primary component (Lehmann et al. 2020). The observed extremal residuals for the primary component are -7.2 ± 0.6 km s^{-1} and +5.8 ± 0.5 km s^{-1}. However, a crucial observation is missing at the expected phase of maximum positive deviation (~ 0.98). Therefore, we cannot yet conclude on the detection of any asymmetric attenuation as an indication of ongoing mass transfer.
- An additional finding regarding AS Eri is the fact that no third light is needed (unlike the alternative solution proposed by VH&W).

ACKNOWLEDGEMENTS

This study is based on data collected by the *Transiting Exoplanet Survey Satellite* (TESS) mission, described by Jenkins et al. (2016) and publicly available from the Mikulski Archive for Space Telescopes

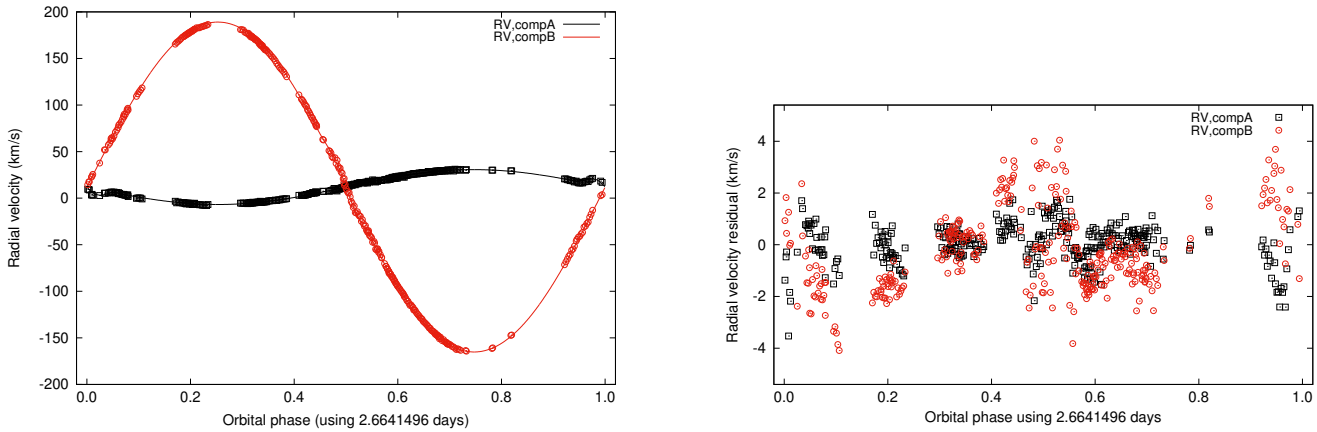

Figure 6. Data and RV model (black and red lines) of AS Eri. Right: The residuals after the model subtraction plotted against the orbital phase.

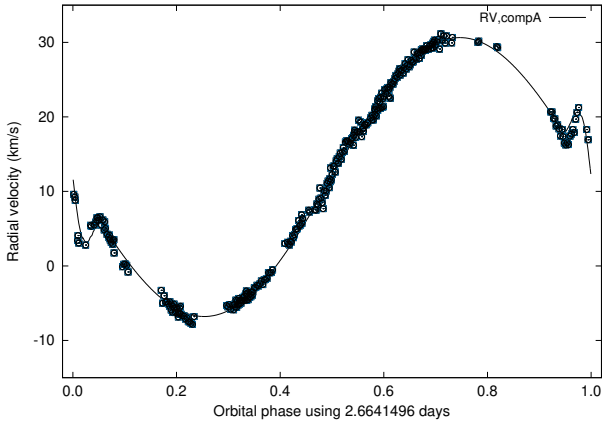

Figure 7. Data and RV model (black line) for the primary component AS Eri A (zoom of Fig. 6 illustrating the fit at the RML phase).

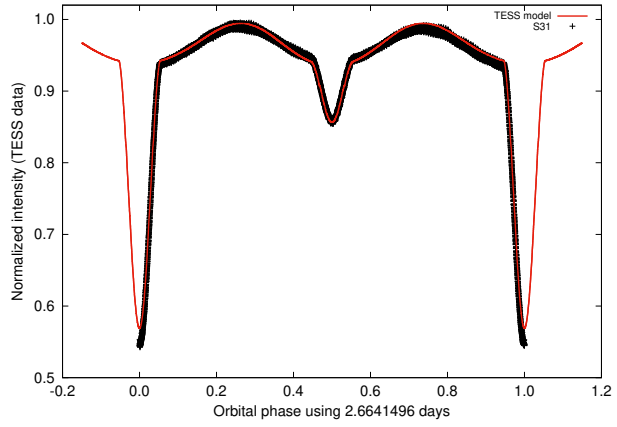

Figure 8. The folded TESS light curve from Sector 31 overplotted with the TESS model (solid red line).

(MAST), as well as on data from the *Microvariability and Oscillations of STars* (MOST) satellite, a Canadian Space Agency mission, jointly operated by Microsatellite Systems Canada Inc. (MSCI), formerly part of Dynacon, Inc., the University of Toronto Institute for Aerospace Studies, and the University of British Columbia with the assistance of the University of Vienna. Funding for the TESS mission is provided by NASA's Science Mission directorate. This study made use of high-resolution spectra obtained with the HERMES échelle spectrograph installed at the *Mercator* telescope operated by the IvS, KULeuven, funded by the Flemish Community, and located at the Observatorio Roque de los Muchachos on the island of La Palma, Spain, as well as with the TCES échelle spectrograph of the *Alfred Jensch* telescope located at the Thüringer Landessternwarte, Tautenburg, Germany. This research also made use of the Lichtenknecker-Database of the BAV, operated by the *Bundesdeutsche Arbeitsgemeinschaft für Veränderliche Sterne e.V. (BAV)*. PL and LV gratefully acknowledge the financial support of the Royal Observatory of Belgium to the HERMES Consortium, as well as the help of the HERMES Consortium observers P. De Cat, N. Dries, M. Hillen, A. Jorissen and S. Goriely. DM and KG thankfully acknowledge the support of the National Astronomical Research Institute of Thailand.

DATA AVAILABILITY

The light curve of AS Eri obtained by the MOST satellite is no longer publicly available. These data will be deposited at the Centre de Données Stellaires, Strasbourg, France. The data collected by the TESS mission are publicly available from the Mikulski Archive for Space Telescopes (MAST) at *https://mast.stsci.edu/portal/Mashup/Clients/Mast/Portal.html*.
The high-resolution spectra acquired with the spectrograph HERMES are available from the HERMES Consortium lead by the Instituut voor Sterrenkunde, University of Leuven, Leuven, Belgium upon specific request. Similarly, the spectra acquired with the TCES spectrograph are available from the Thüringer Landessternwarte, Tautenburg, Germany, upon specific request.

REFERENCES

Aerts C., 2021, Reviews of Modern Physics, 93, 015001
Alicavus F., 2020, arXiv e-prints, p. arXiv:2001.01292
Applegate J. H., 1992, ApJ, 385, 621
Broglia P., 1973, Information Bulletin on Variable Stars, 823, 1
Budding E., Butland R., 2011, MNRAS, 418, 1764
Cheng S. J., Fuller J., Guo Z., Lehmann H., Hambleton K., 2020, ApJ, 903, 122
Eggleton P. P., Kiseleva-Eggleton L., 2002, ApJ, 575, 461
Fuller J., Lai D., 2012, MNRAS, 420, 3126
Gamarova A. Y., Mkrtichian D. E., Kusakin A. V., 2000, Information Bulletin on Variable Stars, 4837, 1
Gamarova A. Y., Mkrtichian D. E., Rodríguez E., Costa V., Lopez-Gonzalez M. J., 2003, in Sterken C., ed., Astronomical Society of the Pacific Conference Series Vol. 292, Interplay of Periodic, Cyclic and Stochastic Variability in Selected Areas of the H-R Diagram. p. 369
Glazunova L. V., Yushchenko A. V., Tsymbal V. V., Mkrtichian D. E., Lee J. J., Kang Y. W., Valyavin G. G., Lee B. C., 2008, AJ, 136, 1736
Guo Z., Gies D. R., Matson R. A., García Hernández A., 2016, ApJ, 826, 69
Horvat M., Conroy K. E., Pablo H., Hambleton K. M., Kochoska A., Giammarco J., Prša A., 2018, ApJS, 237, 26
Hutchings J. B., Hill G., 1971, ApJ, 166, 373
Koch R. H., 1960, AJ, 65, 139
Kreiner J. M., 2004, Acta Astron., 54, 207
Kreiner J. M., 2005, VizieR Online Data Catalog (other), 0050, J/other/AcA/54
Lampens P., 2021, Galaxies, 9, 28
Lehmann H., Tsymbal V., Pertermann F., Tkachenko A., Mkrtichian D. E., A-thano N., 2018, A&A, 615, A131
Lehmann H., Dervişoğlu A., Mkrtichian D. E., Pertermann F., Tkachenko A., Tsymbal V., 2020, A&A, 644, A121
Lindsay E. M., Cillié G. G., 1960, Monthly Notes of the Astronomical Society of South Africa, 19, 150
Mazeh T., Zucker S., 1994, Ap&SS, 212, 349
Mkrtichian D. E., Kusakin A. V., Gamarova A. Y., Nazarenko V., 2002, in Aerts C., Bedding T. R., Christensen-Dalsgaard J., eds, Astronomical Society of the Pacific Conference Series Vol. 259, IAU Colloq. 185: Radial and Nonradial Pulsationsn as Probes of Stellar Physics. p. 96
Mkrtichian D. E., et al., 2004, A&A, 419, 1015
Mkrtichian D. E., et al., 2018, MNRAS, 475, 4745
Narusawa S.-y., 2013, PASJ, 65, 105
Popper D. M., 1973, ApJ, 185, 265
Prša A., Zwitter T., 2005, ApJ, 628, 426
Prša A., Matijevic G., Latkovic O., Vilardell F., Wils P., 2011, PHOEBE: PHysics Of Eclipsing BinariEs (ascl:1106.002)
Prša A., et al., 2016, ApJS, 227, 29
Raskin G., et al., 2011, A&A, 526, A69
Ricker G. R., et al., 2016, in MacEwen H. A., Fazio G. G., Lystrup M., Batalha N., Siegler N., Tong E. C., eds, Society of Photo-Optical Instrumentation Engineers (SPIE) Conference Series Vol. 9904, Space Telescopes and Instrumentation 2016: Optical, Infrared, and Millimeter Wave. p. 99042B, doi:10.1117/12.2232071
Rodríguez E., et al., 2004, MNRAS, 347, 1317
Tempesti P., 1971, Information Bulletin on Variable Stars, 596, 1
Torres G., Andersen J., Giménez A., 2010, A&ARv, 18, 67
Van Hamme W., Wilson R. E., 1984, A&A, 141, 1
Walker G., et al., 2003, PASP, 115, 1023
Wilson R. E., Devinney E. J., 1971, ApJ, 166, 605

APPENDIX A: RADIAL VELOCITIES

APPENDIX B: THE (O-C) DATA

Table A1. Times (BJD), orbital phases and radial velocities of the primary (RV1) and the secondary (RV2) components of AS Eri measured from LP and TLS.

BJD	Site	Phase	RV1	RV2
2455609.398200	LP	0.281206	-3.360	165.429
2455609.402254	LP	0.282728	-3.649	164.712
2455610.354684	LP	0.640227	29.775	-154.801
2455610.358737	LP	0.641748	29.263	-156.470
2455611.377055	LP	0.023978	3.406	95.017
2455611.381108	LP	0.025500	3.527	96.513
2455612.347864	LP	0.388376	5.732	78.090
2455612.351918	LP	0.389898	6.346	76.779
2455613.350182	LP	0.764601	29.445	-147.308
2455613.354236	LP	0.766122	29.289	-146.929
2455614.383140	LP	0.152326	-5.640	180.702
2455614.388062	LP	0.154174	-5.406	181.493
2455615.387072	LP	0.529156	21.065	-80.193
2455615.391126	LP	0.530678	21.357	-81.414
2455616.350056	LP	0.890617	18.317	-46.082
2455616.354109	LP	0.892138	17.380	-44.187
2455617.349968	LP	0.265938	-5.106	172.740
2455617.354021	LP	0.267460	-5.141	172.087
2455618.351279	LP	0.641785	29.987	-156.026
2455618.357069	LP	0.643958	30.298	-157.078
2455619.351054	LP	0.017055	4.133	88.039
2455619.355108	LP	0.018577	3.477	90.128
2455620.375541	LP	0.401601	7.472	63.066
2455620.379594	LP	0.403122	7.241	62.512
2455829.656783	LP	0.956262	4.076	23.735
2455829.660836	LP	0.957783	3.067	25.526
2455829.754237	LP	0.992841	6.472	63.979
2455829.758291	LP	0.994363	6.499	64.923
2455831.577462	LP	0.677197	29.936	-163.572
2455831.581517	LP	0.678719	30.669	-164.281
2455831.712994	LP	0.728069	30.006	-161.374
2455831.717048	LP	0.729591	30.158	-160.663
2455833.614931	LP	0.441970	11.682	16.537
2455833.618985	LP	0.443492	13.146	13.556
2455833.738211	LP	0.488244	17.536	-36.621
2455833.742265	LP	0.489766	17.958	-36.565
2456146.729384	LP	0.970896	2.803	37.673
2456520.733860	LP	0.355168	2.996	110.865
2456971.564850	LP	0.576619	26.458	-120.097
2456972.476582	LP	0.918841	20.592	-17.210
2456972.484800	LP	0.921926	21.253	-12.952
2456972.552707	LP	0.947415	9.615	14.450
2456972.560925	LP	0.950500	8.794	17.428
2456972.638719	LP	0.979700	5.450	51.943
2456972.643117	LP	0.981351	5.292	51.741
2456972.711967	LP	0.007194	5.911	78.301
2457337.546682	LP	0.949554	9.243	17.655
2457337.559634	LP	0.954416	3.418	22.557
2457338.639344	LP	0.359690	3.172	106.353
2457338.644553	LP	0.361645	2.950	104.994
2457338.649761	LP	0.363600	2.816	103.494
2457338.654971	LP	0.365555	3.314	101.296
2457338.660180	LP	0.367511	3.221	99.707
2457338.665388	LP	0.369466	4.056	98.479
2457338.670597	LP	0.371421	3.795	94.935
2457338.675806	LP	0.373376	4.184	93.457
2457338.681015	LP	0.375331	4.897	91.518
2457338.686224	LP	0.377287	4.940	89.244
2457338.691433	LP	0.379242	4.993	86.990
2457338.696642	LP	0.381197	6.094	85.792

Table A1 – *continued*

BJD	Site	phase	RV1	RV2
2457338.701851	LP	0.383152	5.393	83.169
2457338.707060	LP	0.385107	5.505	81.654
2457338.712269	LP	0.387062	6.869	79.767
2457338.717478	LP	0.389018	6.337	78.377
2457341.445190	LP	0.412877	7.568	51.005
2457341.450398	LP	0.414832	7.488	50.215
2457341.455606	LP	0.416787	8.321	48.421
2457341.460815	LP	0.418742	8.166	44.587
2457341.466024	LP	0.420697	8.958	43.283
2457341.471233	LP	0.422652	10.454	51.709
2457341.476441	LP	0.424607	9.104	43.384
2457341.481650	LP	0.426562	8.497	37.378
2457341.486859	LP	0.428518	7.692	40.751
2457341.492068	LP	0.430473	10.093	34.226
2457341.497277	LP	0.432428	9.469	31.822
2457341.502487	LP	0.434383	10.057	32.317
2457341.507695	LP	0.436338	11.077	28.074
2457341.512904	LP	0.438293	11.383	26.739
2457341.518113	LP	0.440249	10.501	20.784
2457341.523322	LP	0.442204	11.304	21.092
2457341.528531	LP	0.444159	11.542	14.770
2457341.533740	LP	0.446114	12.272	10.010
2457341.538949	LP	0.448070	13.380	7.290
2457341.544158	LP	0.450025	13.409	5.496
2457341.549366	LP	0.451980	12.611	5.935
2457341.554575	LP	0.453935	14.091	1.399
2457341.559784	LP	0.455890	14.383	-3.499
2457341.564993	LP	0.457845	13.782	-5.463
2457341.570202	LP	0.459801	14.671	-9.996
2457341.575411	LP	0.461756	15.137	-8.478
2457341.580620	LP	0.463711	14.322	-15.429
2457341.585829	LP	0.465666	15.241	-15.877
2457341.591038	LP	0.467622	15.898	-14.541
2457341.596247	LP	0.469577	15.386	-17.550
2457341.601456	LP	0.471532	16.616	-19.219
2457341.606664	LP	0.473487	16.769	-19.545
2457341.611873	LP	0.475442	16.761	-24.842
2457341.617081	LP	0.477397	16.667	-23.111
2457341.622290	LP	0.479352	16.319	-27.313
2457341.627499	LP	0.481307	16.549	-30.122
2457341.632709	LP	0.483263	17.080	-29.476
2457341.637917	LP	0.485218	17.191	-34.341
2457341.643126	LP	0.487173	16.190	-35.132
2457341.648335	LP	0.489128	18.213	-34.915
2457341.653543	LP	0.491083	17.233	-39.998
2457341.658752	LP	0.493038	17.987	-40.978
2457341.663960	LP	0.494993	18.040	-42.319
2457341.669169	LP	0.496948	19.559	-47.235
2457341.679587	LP	0.500859	19.316	-48.192
2457341.684796	LP	0.502814	17.355	-54.784
2457341.690004	LP	0.504769	18.436	-55.610
2457341.695213	LP	0.506724	18.090	-54.209
2457341.700422	LP	0.508679	18.990	-58.238
2457344.426931	LP	0.532087	21.095	-81.739
2457344.432139	LP	0.534042	22.144	-84.364
2457344.437347	LP	0.535997	22.468	-84.933
2457344.442556	LP	0.537952	22.029	-87.548
2457344.447765	LP	0.539907	22.636	-88.731
2457344.452974	LP	0.541862	23.185	-91.248
2457344.458183	LP	0.543817	22.441	-92.743

Table A1 – *continued*

BJD	Site	phase	RV1	RV2
2457344.463392	LP	0.545772	22.741	-94.489
2457353.498421	TLS	0.937111	18.304	2.608
2457353.506314	TLS	0.940074	16.942	3.844
2457354.352117	TLS	0.257550	-5.145	177.068
2457354.359386	TLS	0.260279	-4.587	175.348
2457354.366653	TLS	0.263007	-4.663	174.078
2457354.373910	TLS	0.265730	-4.358	172.705
2457354.381190	TLS	0.268463	-4.644	171.720
2457354.388459	TLS	0.271191	-4.636	170.684
2457354.395716	TLS	0.273915	-4.225	169.294
2457354.402996	TLS	0.276648	-4.073	167.774
2457354.410252	TLS	0.279372	-3.758	166.073
2457354.417520	TLS	0.282100	-4.007	164.717
2457354.424789	TLS	0.284828	-3.540	163.705
2457354.432057	TLS	0.287556	-3.763	160.919
2457354.439326	TLS	0.290284	-3.491	159.893
2457354.446595	TLS	0.293013	-3.481	158.278
2457354.453863	TLS	0.295741	-2.936	156.553
2457354.461131	TLS	0.298469	-2.890	154.975
2457354.468399	TLS	0.301197	-2.599	152.939
2457354.475668	TLS	0.303926	-2.688	151.425
2457354.482936	TLS	0.306654	-2.417	149.452
2457354.490205	TLS	0.309382	-2.023	147.452
2457354.497472	TLS	0.312110	-2.504	144.743
2457354.504741	TLS	0.314838	-1.861	142.748
2457354.512009	TLS	0.317566	-1.798	140.489
2457354.519278	TLS	0.320295	-1.675	138.771
2457354.526546	TLS	0.323023	-0.914	137.166
2457354.533815	TLS	0.325751	-0.926	135.426
2457354.541082	TLS	0.328479	-0.882	132.880
2457354.548351	TLS	0.331208	-0.527	130.371
2457355.361383	TLS	0.636383	29.182	-154.077
2457355.368651	TLS	0.639111	29.311	-154.904
2457375.332966	TLS	0.132807	-4.809	173.563
2457375.340235	TLS	0.135535	-5.906	175.048
2457375.347502	TLS	0.138263	-5.404	175.481
2457375.354771	TLS	0.140992	-5.659	176.488
2457375.362039	TLS	0.143719	-5.994	177.235
2457375.369307	TLS	0.146448	-5.783	178.804
2457375.376575	TLS	0.149176	-6.853	179.161
2457375.383844	TLS	0.151904	-6.350	180.694
2457375.406100	TLS	0.160258	-6.714	182.877
2457375.413367	TLS	0.162986	-7.122	182.891
2457375.420636	TLS	0.165714	-6.966	183.809
2457375.427903	TLS	0.168442	-7.480	184.081
2457375.435172	TLS	0.171170	-7.508	184.680
2457375.442440	TLS	0.173898	-7.724	185.222
2457375.449708	TLS	0.176627	-7.841	185.664
2457375.457069	TLS	0.179389	-6.795	186.535
2457376.310701	TLS	0.499804	17.985	-46.458
2457376.328558	TLS	0.506507	18.450	-54.962
2457376.335827	TLS	0.509235	18.934	-57.009
2457376.343095	TLS	0.511963	18.951	-60.642
2457376.350363	TLS	0.514691	19.213	-63.685
2457376.364899	TLS	0.520148	19.861	-70.252
2457376.372168	TLS	0.522876	19.581	-73.137
2457376.379436	TLS	0.525604	19.604	-75.721
2457376.386704	TLS	0.528332	20.917	-78.430
2457376.458944	TLS	0.555448	22.742	-102.194
2457376.466213	TLS	0.558176	22.510	-105.662

Table A1 – *continued*

BJD	Site	phase	RV1	RV2
2457380.272952	TLS	0.987053	5.490	57.094
2457380.280221	TLS	0.989781	5.872	59.022
2457380.287488	TLS	0.992509	6.089	61.957
2457380.294757	TLS	0.995237	6.158	63.730
2457380.302025	TLS	0.997965	6.600	66.614
2457380.309293	TLS	0.000694	5.488	70.836
2457380.316561	TLS	0.003422	6.163	73.085
2457380.323829	TLS	0.006150	4.829	75.902
2457380.331097	TLS	0.008878	5.030	79.569
2457380.338366	TLS	0.011606	4.251	81.715
2457380.345622	TLS	0.014330	3.875	84.777
2457380.352890	TLS	0.017058	3.681	87.039
2457380.360158	TLS	0.019786	3.172	89.768
2457380.367426	TLS	0.022514	2.910	92.669
2457380.374695	TLS	0.025242	1.741	94.594
2457380.417493	TLS	0.041307	-0.107	109.325
2457380.424761	TLS	0.044035	0.223	112.006
2457380.432029	TLS	0.046763	0.240	114.234
2457380.439297	TLS	0.049491	0.080	116.235
2457380.446566	TLS	0.052220	-0.813	118.409
2457383.281185	TLS	0.116207	-3.279	165.397
2457383.288454	TLS	0.118935	-5.003	167.190
2457383.295721	TLS	0.121663	-3.999	168.373
2457383.302990	TLS	0.124391	-4.845	169.652
2457383.310257	TLS	0.127119	-4.761	171.143
2457383.317526	TLS	0.129847	-5.085	172.819
2457383.324793	TLS	0.132575	-5.414	173.543
2457383.332062	TLS	0.135304	-5.088	174.355
2457383.339330	TLS	0.138032	-6.221	175.845
2457383.346598	TLS	0.140760	-5.129	177.219
2457383.353866	TLS	0.143488	-6.268	178.076
2457383.361135	TLS	0.146216	-5.511	178.839
2457383.368402	TLS	0.148944	-6.460	179.934
2457383.375671	TLS	0.151672	-6.432	180.890
2457383.382938	TLS	0.154400	-6.475	181.327
2457383.390207	TLS	0.157128	-6.691	182.896
2457384.342400	TLS	0.514538	19.237	-64.151
2457384.365152	TLS	0.523079	20.211	-73.230
2457384.372421	TLS	0.525807	20.016	-76.378
2457384.379688	TLS	0.528535	20.347	-78.820
2457384.386957	TLS	0.531263	20.136	-81.462
2457384.394224	TLS	0.533991	20.857	-84.197
2457384.401493	TLS	0.536719	21.168	-86.583
2457384.408760	TLS	0.539447	21.164	-89.213
2457384.416029	TLS	0.542176	21.257	-91.721
2457384.423297	TLS	0.544904	21.368	-94.247
2457385.282625	TLS	0.867456	20.684	-71.469
2457385.289893	TLS	0.870185	20.666	-68.330
2457385.297161	TLS	0.872912	19.794	-65.344
2457385.304429	TLS	0.875641	19.745	-62.257
2457385.311697	TLS	0.878369	18.785	-60.383
2457385.318966	TLS	0.881097	18.924	-55.922
2457385.326233	TLS	0.883825	18.405	-54.660
2457385.333502	TLS	0.886553	17.444	-51.436
2457385.353524	TLS	0.894068	16.490	-41.912
2457385.360791	TLS	0.896796	16.251	-40.941
2457385.368060	TLS	0.899525	16.543	-38.327
2457385.375327	TLS	0.902252	16.283	-36.770
2457385.382596	TLS	0.904981	17.422	-30.967
2457385.389863	TLS	0.907709	17.708	-29.899

Table A1 – *continued*

BJD	Site	phase	RV1	RV2
2457385.397132	TLS	0.910437	18.316	-27.198
2457385.404400	TLS	0.913165	17.889	-25.624
2457385.411668	TLS	0.915893	19.695	-20.508
2457386.280808	TLS	0.242129	-5.316	180.936
2457386.288076	TLS	0.244857	-5.489	180.938
2457386.295333	TLS	0.247581	-5.170	180.598
2457386.302601	TLS	0.250309	-5.826	178.172
2457386.309869	TLS	0.253037	-5.305	177.435
2457386.317137	TLS	0.255765	-5.881	176.531
2457386.326037	TLS	0.259106	-5.528	174.919
2457386.333304	TLS	0.261834	-5.555	173.143
2457386.340573	TLS	0.264562	-5.244	173.563
2457386.347840	TLS	0.267290	-4.614	171.926
2457386.355109	TLS	0.270018	-5.004	170.271
2457386.362377	TLS	0.272746	-4.570	169.429
2457386.369645	TLS	0.275474	-4.650	168.304
2457386.376914	TLS	0.278203	-4.624	165.802
2457386.384181	TLS	0.280930	-4.622	163.921
2457380.446566	TLS	0.052220	-0.813	118.409
2457383.281185	TLS	0.116207	-3.279	165.397
2457383.288454	TLS	0.118935	-5.003	167.190
2457383.295721	TLS	0.121663	-3.999	168.373
2457383.302990	TLS	0.124391	-4.845	169.652
2457383.310257	TLS	0.127119	-4.761	171.143
2457383.317526	TLS	0.129847	-5.085	172.819
2457383.324793	TLS	0.132575	-5.414	173.543
2457383.332062	TLS	0.135304	-5.088	174.355
2457383.339330	TLS	0.138032	-6.221	175.845
2457383.346598	TLS	0.140760	-5.129	177.219
2457383.353866	TLS	0.143488	-6.268	178.076
2457383.361135	TLS	0.146216	-5.511	178.839
2457383.368402	TLS	0.148944	-6.460	179.934
2457383.375671	TLS	0.151672	-6.432	180.890
2457383.382938	TLS	0.154400	-6.475	181.327
2457383.390207	TLS	0.157128	-6.691	182.896
2457384.342400	TLS	0.514538	19.237	-64.151
2457384.365152	TLS	0.523079	20.211	-73.230
2457384.372421	TLS	0.525807	20.016	-76.378
2457384.379688	TLS	0.528535	20.347	-78.820
2457384.386957	TLS	0.531263	20.136	-81.462
2457384.394224	TLS	0.533991	20.857	-84.197
2457384.401493	TLS	0.536719	21.168	-86.583
2457384.408760	TLS	0.539447	21.164	-89.213
2457384.416029	TLS	0.542176	21.257	-91.721
2457384.423297	TLS	0.544904	21.368	-94.247
2457385.282625	TLS	0.867456	20.684	-71.469
2457385.289893	TLS	0.870185	20.666	-68.330
2457385.297161	TLS	0.872912	19.794	-65.344
2457385.304429	TLS	0.875641	19.745	-62.257
2457385.311697	TLS	0.878369	18.785	-60.383
2457385.318966	TLS	0.881097	18.924	-55.922
2457385.326233	TLS	0.883825	18.405	-54.660
2457385.333502	TLS	0.886553	17.444	-51.436
2457385.353524	TLS	0.894068	16.490	-41.912
2457385.360791	TLS	0.896796	16.251	-40.941
2457385.368060	TLS	0.899525	16.543	-38.327
2457385.375327	TLS	0.902252	16.283	-36.770
2457385.382596	TLS	0.904981	17.422	-30.967
2457385.389863	TLS	0.907709	17.708	-29.899
2457385.397132	TLS	0.910437	18.316	-27.198

Table A1 – *continued*

BJD	Site	phase	RV1	RV2
2457385.404400	TLS	0.913165	17.889	-25.624
2457385.411668	TLS	0.915893	19.695	-20.508
2457386.280808	TLS	0.242129	-5.316	180.936
2457386.288076	TLS	0.244857	-5.489	180.938
2457386.295333	TLS	0.247581	-5.170	180.598
2457386.302601	TLS	0.250309	-5.826	178.172
2457386.309869	TLS	0.253037	-5.305	177.435
2457386.317137	TLS	0.255765	-5.881	176.531
2457386.326037	TLS	0.259106	-5.528	174.919
2457386.333304	TLS	0.261834	-5.555	173.143
2457386.340573	TLS	0.264562	-5.244	173.563
2457386.347840	TLS	0.267290	-4.614	171.926
2457386.355109	TLS	0.270018	-5.004	170.271
2457386.362377	TLS	0.272746	-4.570	169.429
2457386.369645	TLS	0.275474	-4.650	168.304
2457386.376914	TLS	0.278203	-4.624	165.802
2457386.384181	TLS	0.280930	-4.622	163.921

This paper has been typeset from a TEX/LATEX file prepared by the author.

Table B1. Times of minima and their corresponding O-C residuals.

Time of min. [HJD]	Type	Cycle	(O-C) [d]	Meth.	Observer	Source	Error
2415957.885	P	-15246	-0.07129	pg	S.Gaposchkin	HB 918.13	—
2416775.814	P	-14939	-0.03639	pg	S.Gaposchkin	HB 918.13	—
2417140.855	P	-14802	0.01603	pg	S.Gaposchkin	HB 918.13	—
2417521.778	P	-14659	-0.03444	pg	S.Gaposchkin	HB 918.13	—
2418560.825	P	-14269	-0.00601	pg	S.Gaposchkin	HB 918.13	—
2418592.796	P	-14257	-0.00481	pg	S.Gaposchkin	HB 918.13	—
2418600.785	P	-14254	-0.00826	pg	S.Gaposchkin	HB 918.13	—
2420417.794	P	-13572	0.05031	pg	S.Gaposchkin	HB 918.13	—
2421576.612	P	-13137	-0.03701	pg	S.Gaposchkin	HB 918.13	—
2423004.599	P	-12601	-0.03451	pg	S.Gaposchkin	HB 918.13	—
2426217.580	P	-11395	-0.01862	pg	C.Hoffmeister	AN 253.199	—
2426273.553	P	-11374	0.00722	pg	C.Hoffmeister	AN 253.199	—
2426955.563	P	-11118	-0.00522	pg	C.Hoffmeister	AN 253.199	—
2426979.517	P	-11109	-0.02857	pg	C.Hoffmeister	AN 253.199	—
2428924.358	P	-10379	-0.01720	Vis	F.Lause	AN 277.41	—
2428948.435	P	-10370	0.08245	Vis	F.Lause	AN 277.41	—
2428956.329	P	-10367	-0.01600	Vis	F.Lause	AN 277.41	—
2428964.322	P	-10364	-0.01545	Vis	F.Lause	AN 277.41	—
2429230.747	P	-10264	-0.00547	pg	S.Gaposchkin	HB 918.13	—
2429571.773	P	-10136	0.00930	pg	S.Gaposchkin	HB 918.13	—
2429571.816	P	-10136	0.05230	pg	S.Gaposchkin	HB 918.13	—
2429763.910	F	-10064	0.32749	pg	S.Gaposchkin	HA 113.74	—
2429896.815	P	-10014	0.02498	pg	S.Gaposchkin	HB 918.13	—
2429912.779	P	-10008	0.00408	pg	S.Gaposchkin	HB 918.13	—
2429952.779	P	-9993	0.04183	pg	S.Gaposchkin	HB 918.13	—
2430293.749	P	-9865	0.00061	pg	S.Gaposchkin	HB 918.13	—
2430325.674	P	-9853	-0.04420	pg	S.Gaposchkin	HB 918.13	—
2431055.696	P	-9579	0.00066	pg	S.Gaposchkin	HB 918.13	—
2432230.591	P	-9138	0.00543	Vis	A.Soloviev	AC 62.9	—
2433298.834	F	-8737	-0.07579	pg	S.Kaho	BTOK 30.278	—
2433597.293	P	-8625	-0.00161	pg	G.S.Filatov	BTAD 35.33	—
2433647.809	F	-8606	-0.10447	pg	S.Kaho	BTOK 49.385	—
2435432.894	P	-7936	-0.00009	E/?	R.H.Koch	AJ 65.145	—
2435456.868	P	-7927	-0.00344	E/?	R.H.Koch	AJ 65.145	—
2435478.187	P	-7919	0.00236	pg	G.S.Filatov	BTAD 35.33	—
2435510.167	P	-7907	0.01256	pg	G.S.Filatov	BTAD 35.33	—
2435542.138	P	-7895	0.01376	pg	G.S.Filatov	BTAD 35.33	—
2435765.9102	P	-7811	-0.00266	E/?	R.H.Koch	AJ 65.145	—
2435776.567	P	-7807	-0.00246	E/Y	E.M.Lindsay	MNSSA 19.150	0.002
2435776.569	P	-7807	-0.00046	E/B	E.M.Lindsay	MNSSA 19.150	0.001
2435792.554	P	-7801	-0.00036	E/Y	E.M.Lindsay	MNSSA 19.150	0.0005
2435792.555	P	-7801	0.00064	E/B	E.M.Lindsay	MNSSA 19.150	0.0005
2435811.180	P	-7794	-0.02341	pg	G.S.Filatov	BTAD 35.33	—
2440566.710	P	-6009	-0.00148	Vis	M.Baldwin	IBVS 795	—
2441616.409	P	-5615	0.02235	Vis	K.Locher	BBS 6	—
2441688.313	P	-5588	-0.00570	Vis	K.Locher	BBS 7	—
2441728.308	P	-5573	0.02704	Vis	K.Locher	BBS 8	—
2442426.284	P	-5311	-0.00430	Vis	R.Germann	BBS 20	—
2446707.543	P	-3704	-0.03464	Vis	A.Paschke	BBS 82	—
2447477.466	P	-3415	-0.05104	Vis	A.Paschke	BBS 90	—
2449374.3941	P	-2703	0.00213	E/B	E.Blaettler	BBS 106	0.0012
2450096.376	P	-2432	-0.00066	Vis	M.Kohl	BBS 111	—
2451098.105	P	-2056	0.00787	C/Rc	S.Kiyota	VSB 47	—
2452621.992	P	-1484	0.00097	Vis	Kanai	VSB 40	—
2452637.970	P	-1478	-0.00593	Vis	Kanai	VSB 40	—
2452637.9797	P	-1478	0.00377	E/R	Nagai	VSB 40	—
2453296.035	P	-1231	0.01397	Vis	Kanai	VSB 43	—
2453306.6756	P	-1227	-0.00203	C/I	W.Ogloza et al.	IBVS 5843	0.0023
2453375.949	P	-1201	0.00347	Vis	Kanai	VSB 44	—

Table B1 – *continued*

Time of min. [HJD]	Type	Cycle	(O-C) [d]	Meth.	Observer	Source	Error
2453391.938	P	-1195	0.00757	Vis	Kanai	VSB 44	—
2453764.916	P	-1055	0.00454	Vis	K.Nagai et al.	VSB 45	—
2454097.9306	P	-930	0.00037	E/V	K.Nagai et al.	VSB 45	—
2454113.9165	P	-924	0.00137	C/Ic	K.Nakajima	VSB 46	—
2454454.926	P	-796	-0.00035	Vis	K.Kanai	VSB 46	—
2455480.620	P	-411	-0.00417	C/?	A.Paschke	OEJV 130	0.004
2455866.925	P	-266	-0.00095	C/V	R.Diethelm	IBVS 6011	0.0003
2456575.589	P	0	-0.00090	M	MOST	This work	0.001
2456576.919	S	0.5	-0.00297	M	MOST	This work	0.003
2456578.256	P	1	0.00195	M	MOST	This work	0.001
2456579.585	S	1.5	-0.00112	M	MOST	This work	0.003
2456580.914	P	2	-0.00420	M	MOST	This work	0.001
2456584.914	S	3.5	-0.00042	M	MOST	This work	0.001
2456588.908	P	5	-0.00265	M	MOST	This work	0.002
2456590.241	S	5.5	-0.00172	M	MOST	This work	0.001
2456591.574	P	6	-0.00080	M	MOST	This work	0.001
2456594.241	P	7	0.00205	M	MOST	This work	0.001
2456595.578	S	7.5	0.00698	M	MOST	This work	0.003
2456596.906	P	8	0.00290	M	MOST	This work	0.001
2456598.239	S	8.5	0.00383	M	MOST	This work	0.003
2456602.228	P	10	-0.00340	M	MOST	This work	0.001
2456603.563	S	10.5	-0.00047	M	MOST	This work	0.002
2456604.894	P	11	-0.00155	M	MOST	This work	0.001
2456608.896	S	12.5	0.00423	M	MOST	This work	0.002
2456610.227	P	13	0.00315	M	MOST	This work	0.001
2456611.556	S	13.5	0.00008	M	MOST	This work	0.001
2456612.887	P	14	-0.00100	M	MOST	This work	0.001
2456614.219	S	14.5	-0.00107	M	MOST	This work	0.003
2456615.555	P	15	0.00285	M	MOST	This work	0.002
2456935.24955	P	135	-0.00062	C/V	Siding Springs	unpub.	—
2456959.252	P	144	0.02448	Vis	K.Kanai	VSB 59	—
2456963.2171	S	145.5	-0.00665	C/V	Siding Springs	unpub.	—
2456971.2199	S	148.5	0.00370	C/V	Perth Obs.	unpub.	—
2456972.54823	P	149	-0.00007	C/V	Van.Cauteren	IBVS 6230	0.0002
2456975.20966	P	150	-0.00272	C/V	Siding Springs	unpub.	—
2456975.226	P	150	0.01358	Vis	K.Kanai	VSB 59	—
2457276.277	P	263	0.01561	Vis	K.Nagai et al.	VSB 61	—
2457308.246	P	275	0.01481	Vis	K.Nagai et al.	VSB 61	—
2457332.210	P	284	0.00145	Vis	K.Nagai et al.	VSB 61	—
2458411.1898	P	689	0.00043	T	TESS	This work	0.0001
2458412.5216	S	689.5	0.00016	T	TESS	This work	0.0003
2458413.8539	P	690	0.00038	T	TESS	This work	0.0001
2458415.1864	S	690.5	0.00081	T	TESS	This work	0.0003
2458416.5180	P	691	0.00033	T	TESS	This work	0.0001
2458417.8498	S	691.5	0.00006	T	TESS	This work	0.0003
2458421.8460	P	693	0.00003	T	TESS	This work	0.0001
2458423.1788	S	693.5	0.00076	T	TESS	This work	0.0003
2458425.8425	S	694.5	0.00031	T	TESS	This work	0.0003
2458427.1746	P	695	0.00033	T	TESS	This work	0.0001
2458428.5066	S	695.5	0.00026	T	TESS	This work	0.0003
2458429.8388	P	696	0.00038	T	TESS	This work	0.0001
2458431.1713	S	696.5	0.00081	T	TESS	This work	0.0003
2458432.5031	P	697	0.00053	T	TESS	This work	0.0001
2458433.8356	S	697.5	0.00096	T	TESS	This work	0.0003
2458435.1673	P	698	0.00058	T	TESS	This work	0.0001
2458436.5004	S	698.5	0.00161	T	TESS	This work	0.0003
2458437.8301	P	699	-0.00077	C/V	Cerro Tololo	unpub.	—
2459145.1633	S	964.5	0.00056	T	TESS	This work	0.0003
2459146.4942	P	965	-0.00062	T	TESS	This work	0.0001

Table B1 – *continued*

Time of min. [HJD]	Type	Cycle	(O-C) [d]	Meth.	Observer	Source	Error
2459147.8279	S	965.5	0.00101	T	TESS	This work	0.0002
2459149.1585	P	966	-0.00047	T	TESS	This work	0.0001
2459150.4915	S	966.5	0.00046	T	TESS	This work	0.0003
2459151.8226	P	967	-0.00052	T	TESS	This work	0.0001
2459153.1559	S	967.5	0.00071	T	TESS	This work	0.0002
2459154.4868	P	968	-0.00047	T	TESS	This work	0.0001
2459155.8201	S	968.5	0.00076	T	TESS	This work	0.0002
2459157.1508	P	969	-0.00062	T	TESS	This work	0.0001
2459159.8150	P	970	-0.00057	T	TESS	This work	0.0001
2459161.1480	S	970.5	0.00036	T	TESS	This work	0.0002
2459162.4793	P	971	-0.00042	T	TESS	This work	0.0001
2459163.8121	S	971.5	0.00031	T	TESS	This work	0.0003
2459165.1433	P	972	-0.00057	T	TESS	This work	0.0001
2459166.4765	S	972.5	0.00056	T	TESS	This work	0.0003
2459167.8076	P	973	-0.00042	T	TESS	This work	0.0001
2459169.1407	S	973.5	0.00061	T	TESS	This work	0.0002